Effect of Fe-doping induced by valence modulation engineering on nickel hydroxylfluoride cathode of hybrid supercapacitors

Yutong Zhao[a], Zeshuo Meng[a], Jian Xu[a], Zhengyan Du[a], Zeyu Hao[a], Shulong Wang[a], Hongwei Tian[a, *], Zhiqiang Niu[b], Dawei Su[c]

[a] Key Laboratory of Automobile Materials of MOE, School of Materials Science and Engineering, Jilin University, Changchun, 130012, China

E-mail: tianhw@jlu.edu.cn (H. Tian)

[b] Key Laboratory of Advanced Energy Materials Chemistry (Ministry of Education), Nankai University, Tianjin, 300071, China

[c] Applied Chemistry and Environment Science, School of Science, STEM College, RMIT University, Melbourne VIC 3000, Australia.

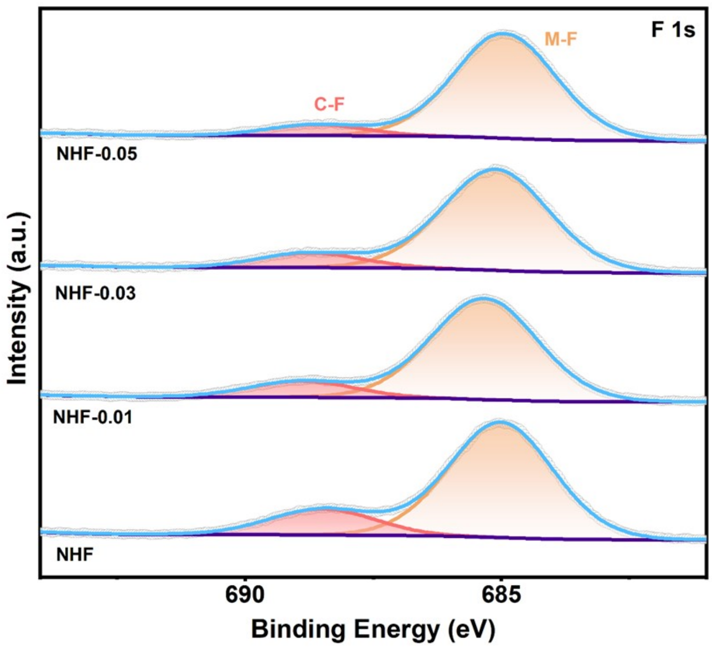

Figure S1. F 1s XPS spectra of NHF–x.

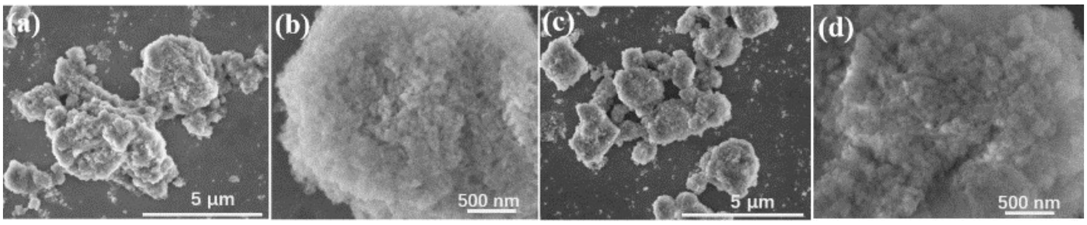

Figure S2.SEM images of (a), (b) NHF–0.01 and (e), (f) NHF–0.05.

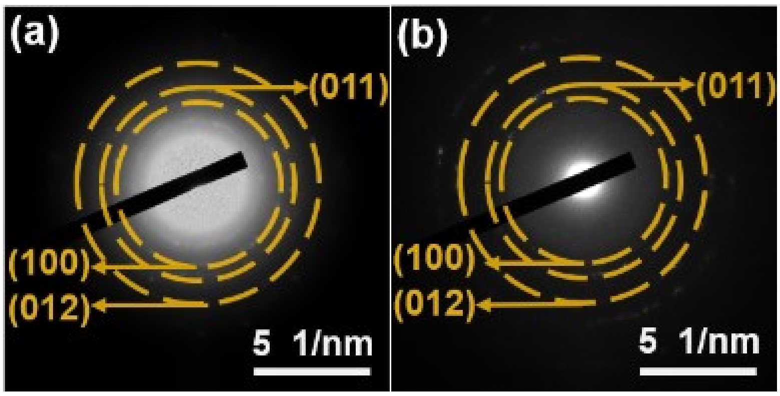

Figure S3. Selected area electron diffraction (SAED) images of (a) NHF and (b) NHF–0.03.

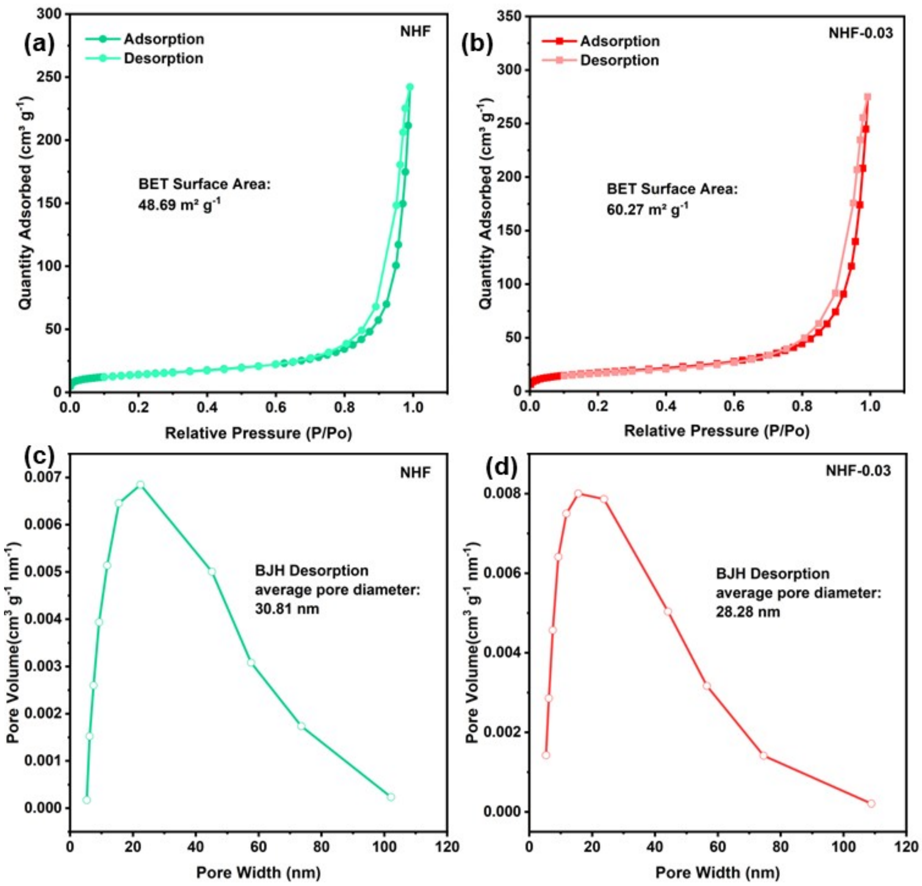

Figure S4.Nitrogen sorption-desorption isotherms of (a) NHF , (b) NHF -0.03. pore size distributions of (c) NHF, (d) NHF -0.03.

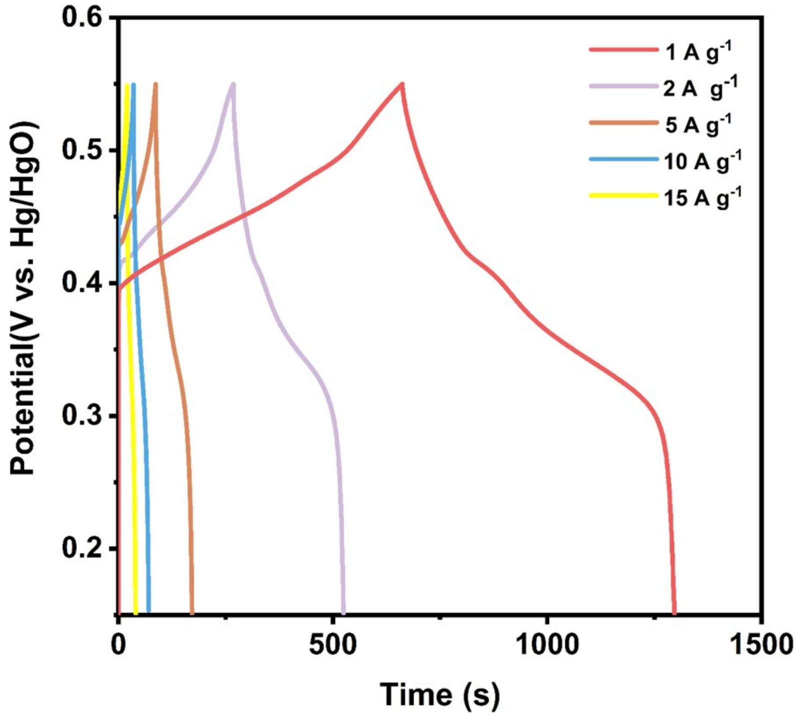

Figure S5.GCD curves of NHF–0.03 at different current densities.

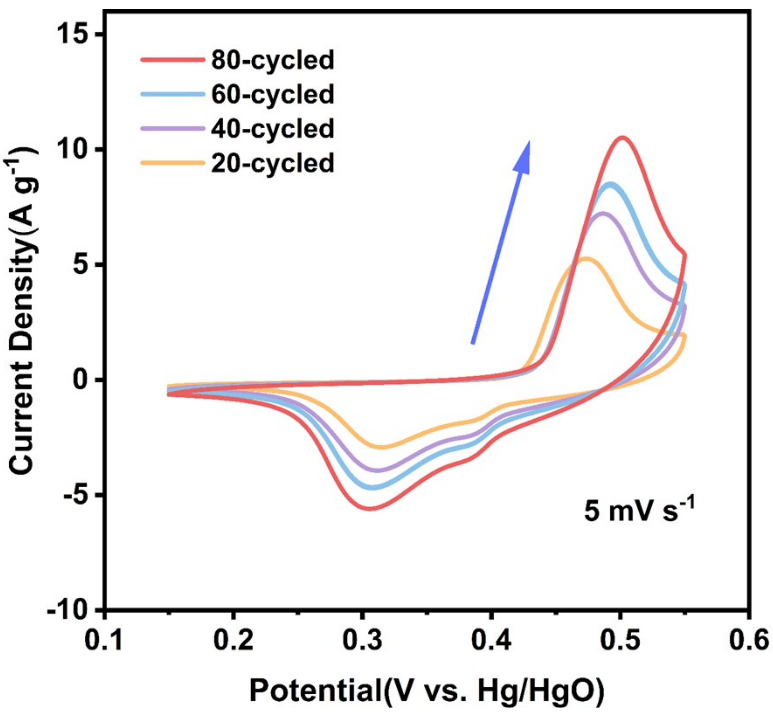

Figure S6. CV cycles of NHF-0.03 of different numbers.

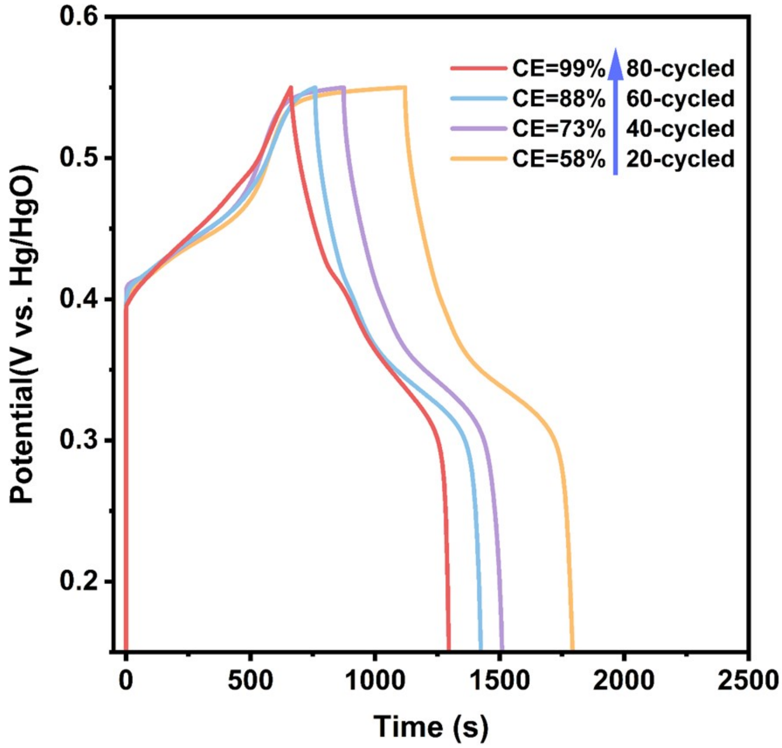

Figure S7. GCD curves of NHF-0.03 of different numbers of CV cycles.

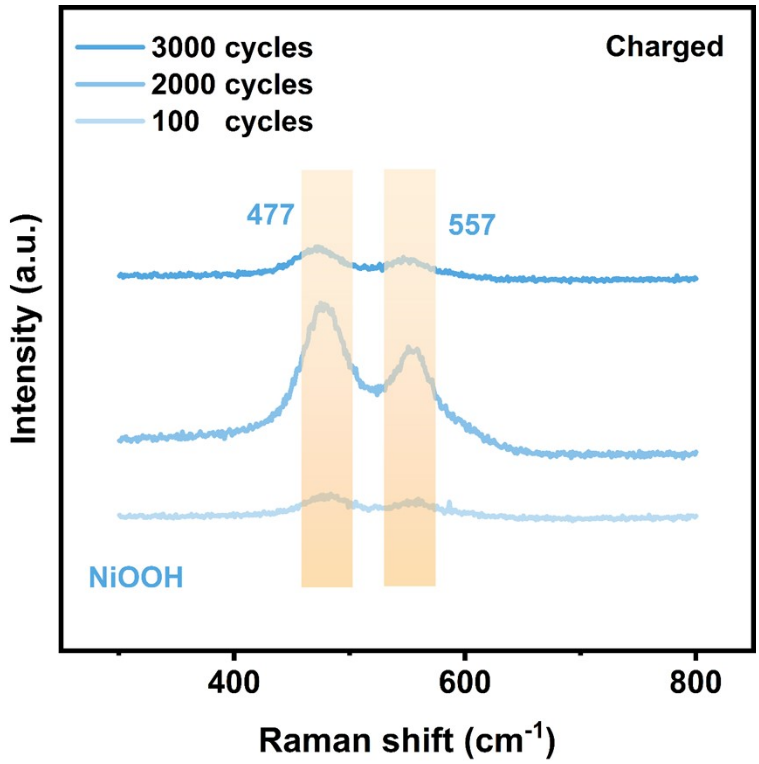

Figure S8. The Raman spectra of NHF-0.03 in the state of charged after different number of cycles.

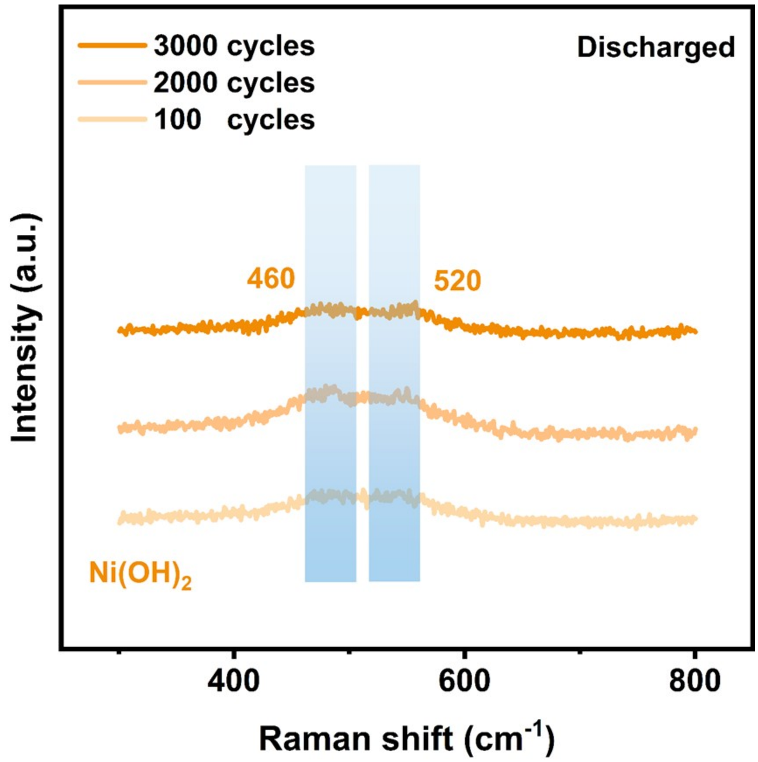

Figure S9. The Raman spectra of NHF-0.03 in the state of discharged after different number of cycles.

At the beginning of the cycle, the electrode material does not have a complete phase transition and is still in the activation stage, so the NiOOH content in the charging state is insufficient and the characteristic peaks of the Raman spectra are not obvious[1, 2]. Similarly, the characteristic peaks of Raman spectra of $Ni(OH)_2$ in the discharged state are not obvious[3]. During the stabilization phase of the cycle, the phase transition is complete and the electrode material can be well transformed between NiOOH and $Ni(OH)_2$ during charging and discharging, and the presence of the two substances can be clearly seen in the Raman spectra. After stabilisation, the electrode capacity decreases again, which can be attributed to the structural collapse and poorer crystallinity of the electrode material after a long cycling process, resulting in poorer energy storage performance than in the stabilisation phase[4-7].

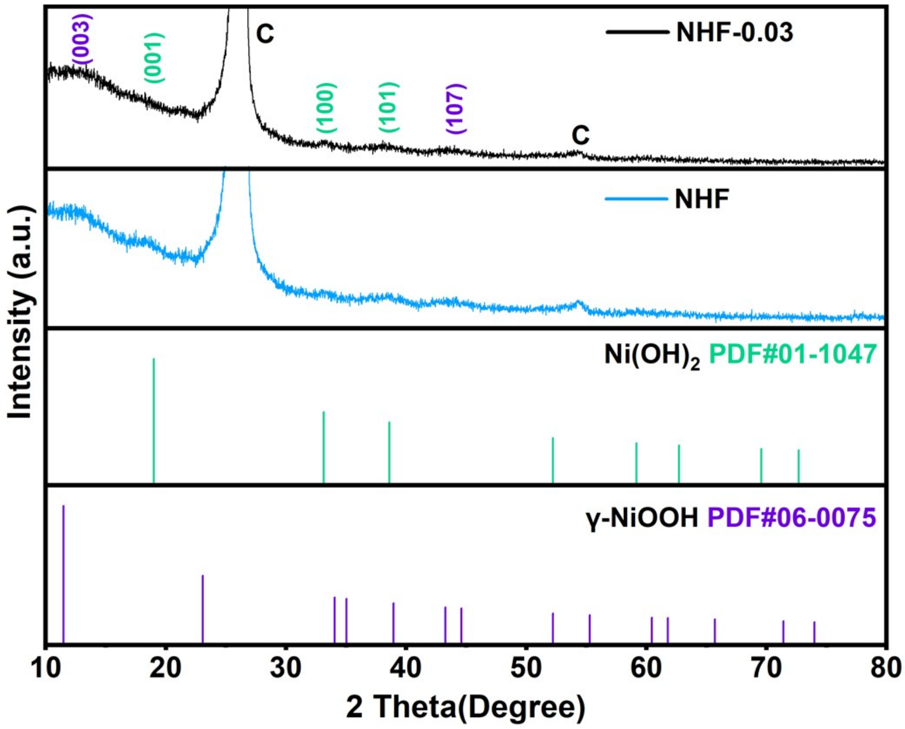

Figure S10.XRD pattern of NHF–x after long-term cycling.

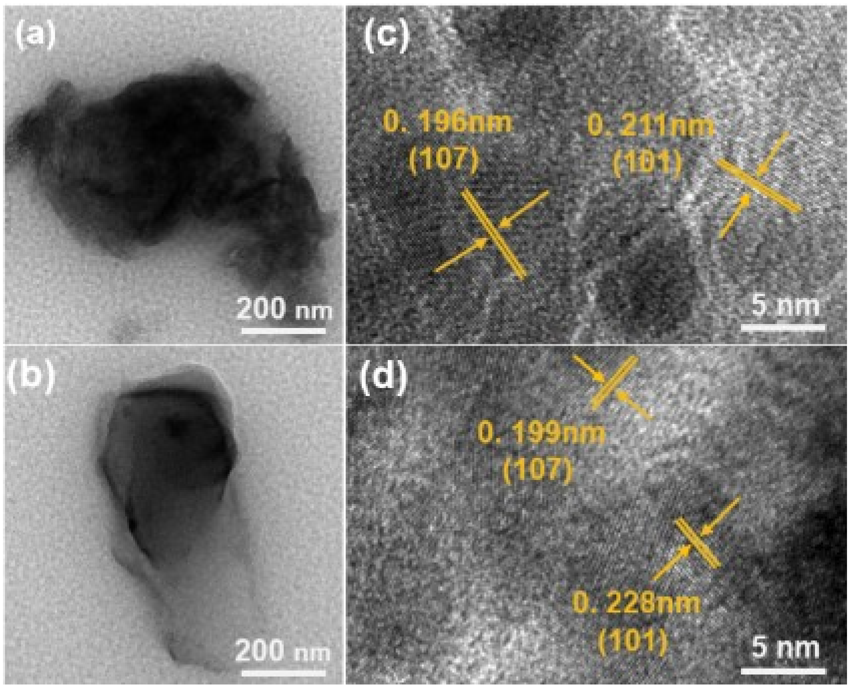

Figure S11.TEM images of (a)NHF, (b) NHF–0.03, and HRTEM images of (c) NHF, (d) NHF–0.03 after long-term cycling.

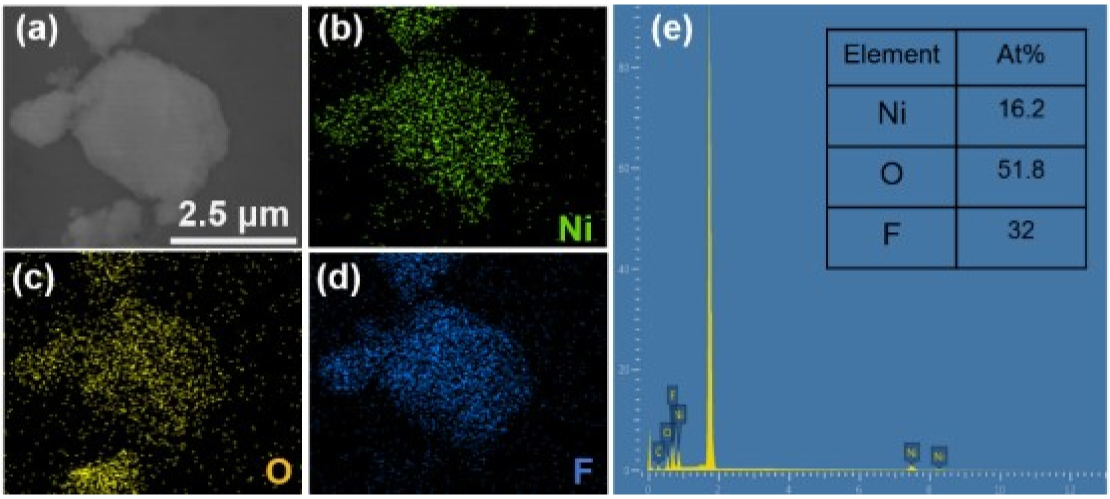

Figure S12. (a) SEM images, and (b-e) Element mapping images of NHF.

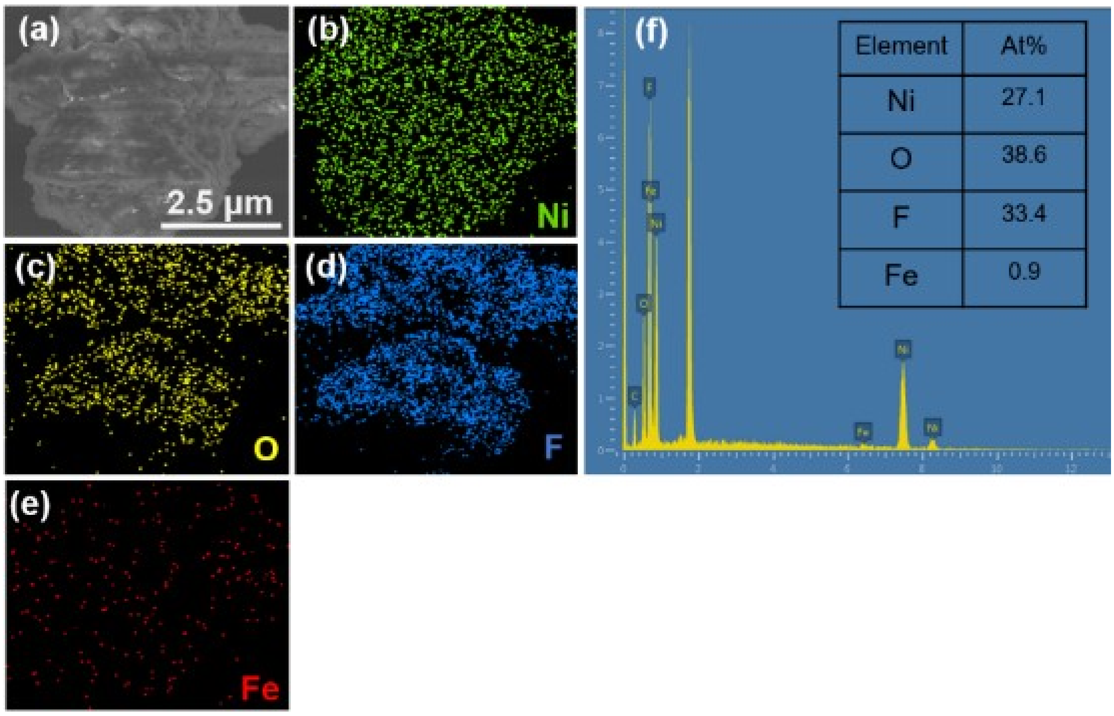

Figure S13. (a) SEM images, and (b-f) Element mapping images of NHF–0.03.

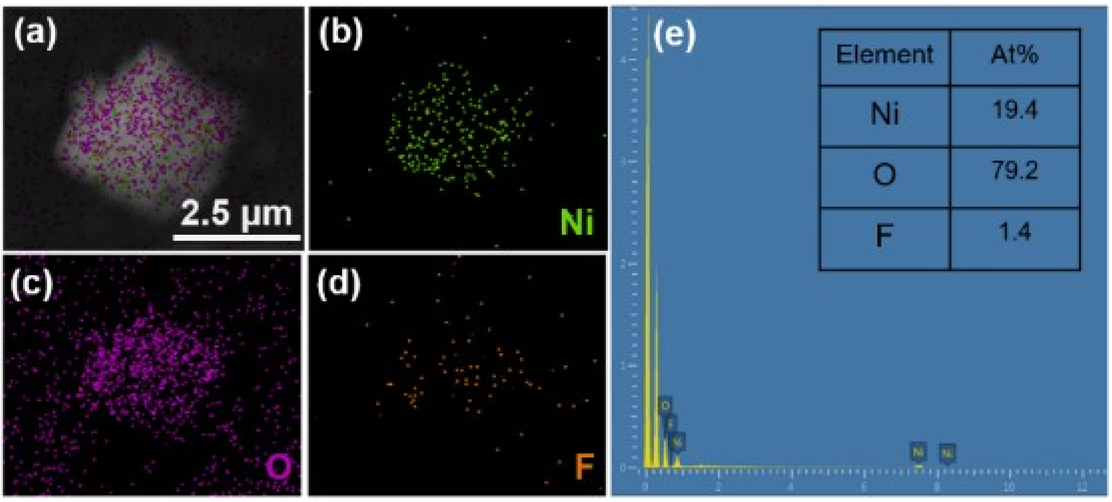

Figure S14. (a) SEM images, and (b-e) Element mapping images of NHF after long-term cycling.

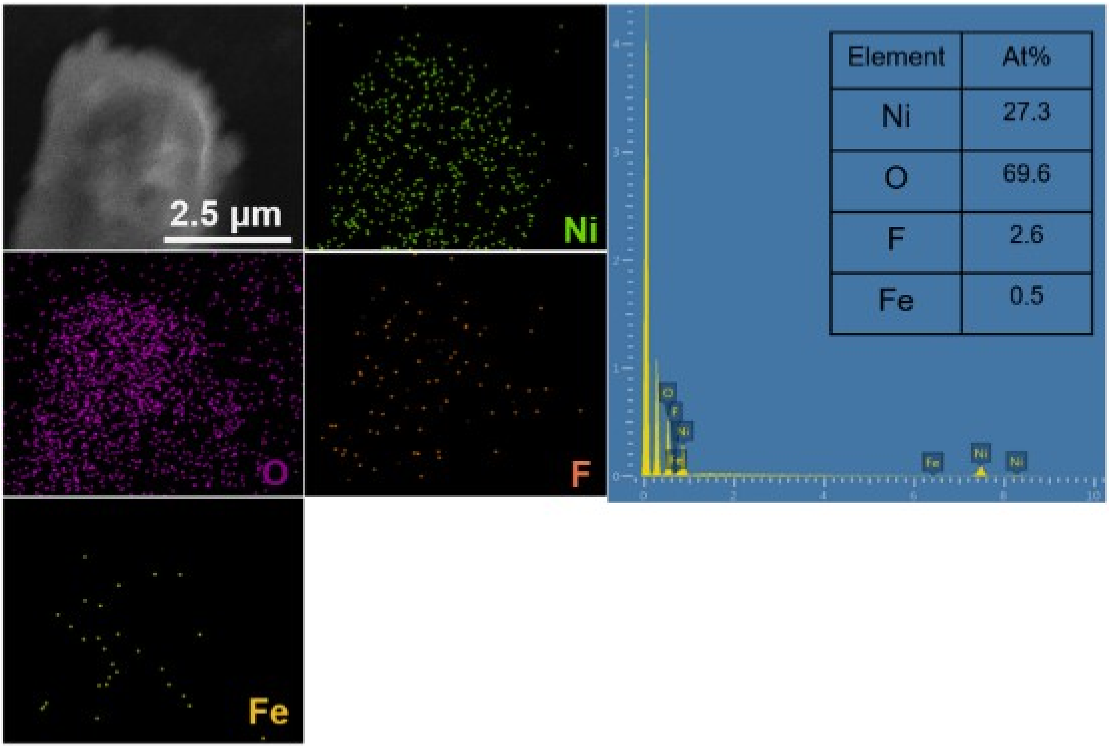

Figure S15. (a) SEM images, and (b-e) Element mapping images of NHF–0.03 after long-term cycling.

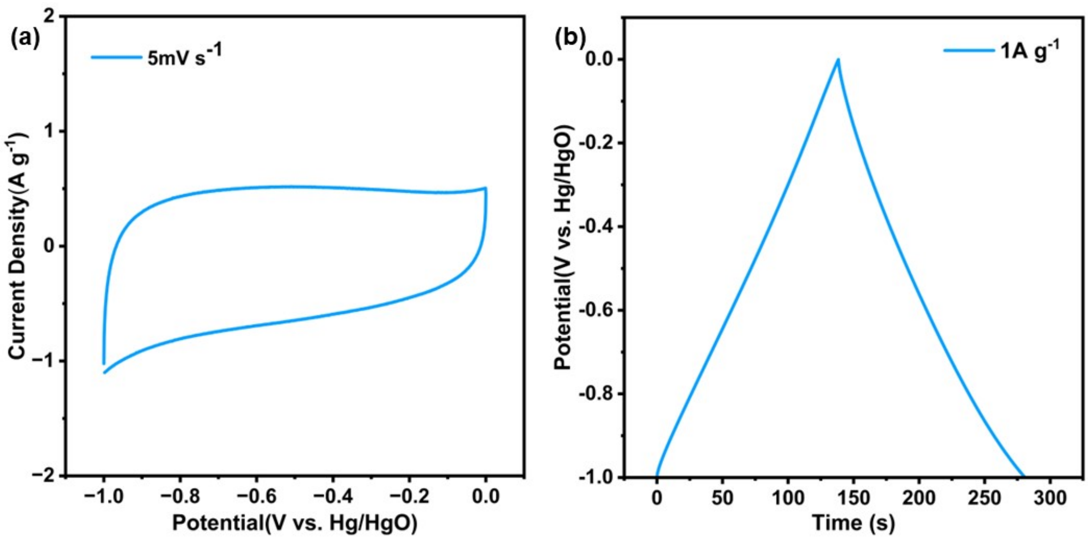

Figure S16. (a) CV curves and (b) GCD curves spectra of AC.

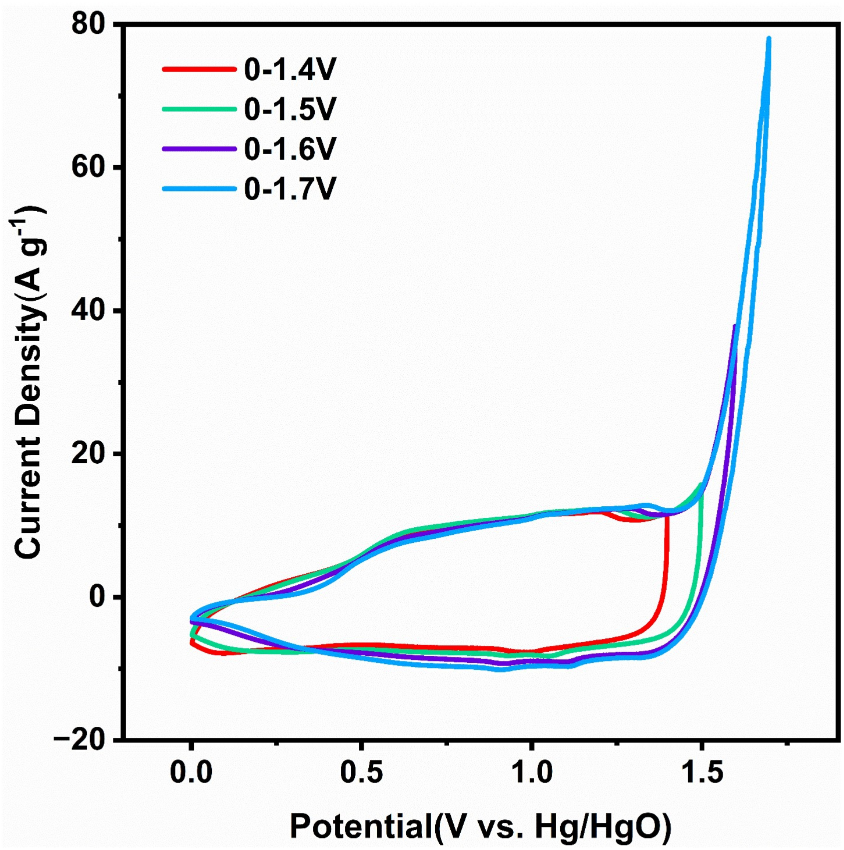

Figure S17. CV plots (at 5 mV s^{-1}) of NHF-0.03//AC device at various potential windows.

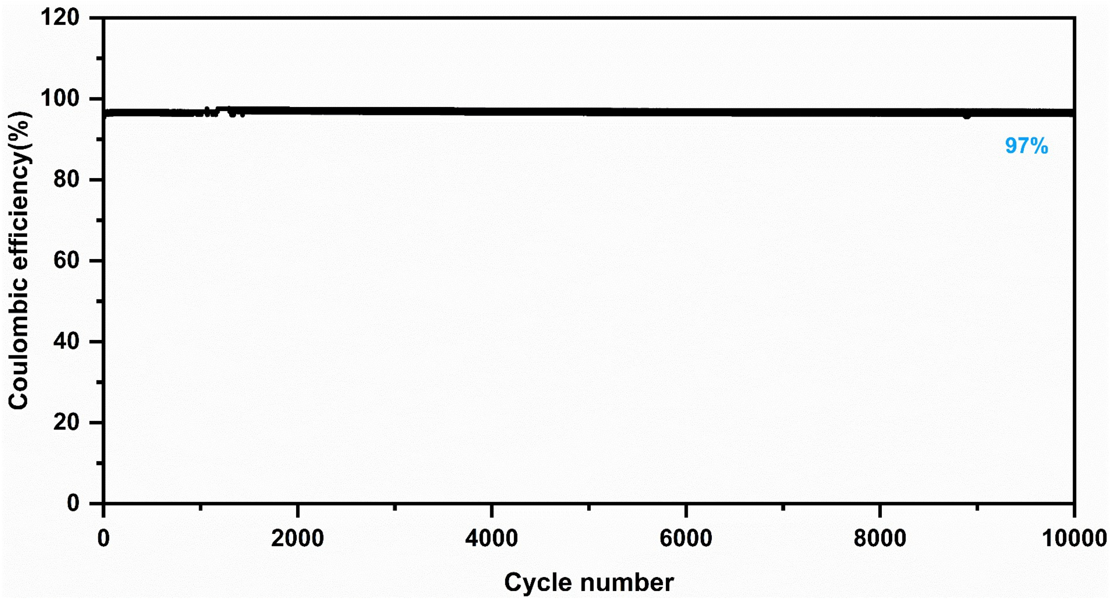

Figure S18. Coulombic efficiency for 10,000 cycles at 15 A g^{-1} of the NHF-0.03//AC ASC.

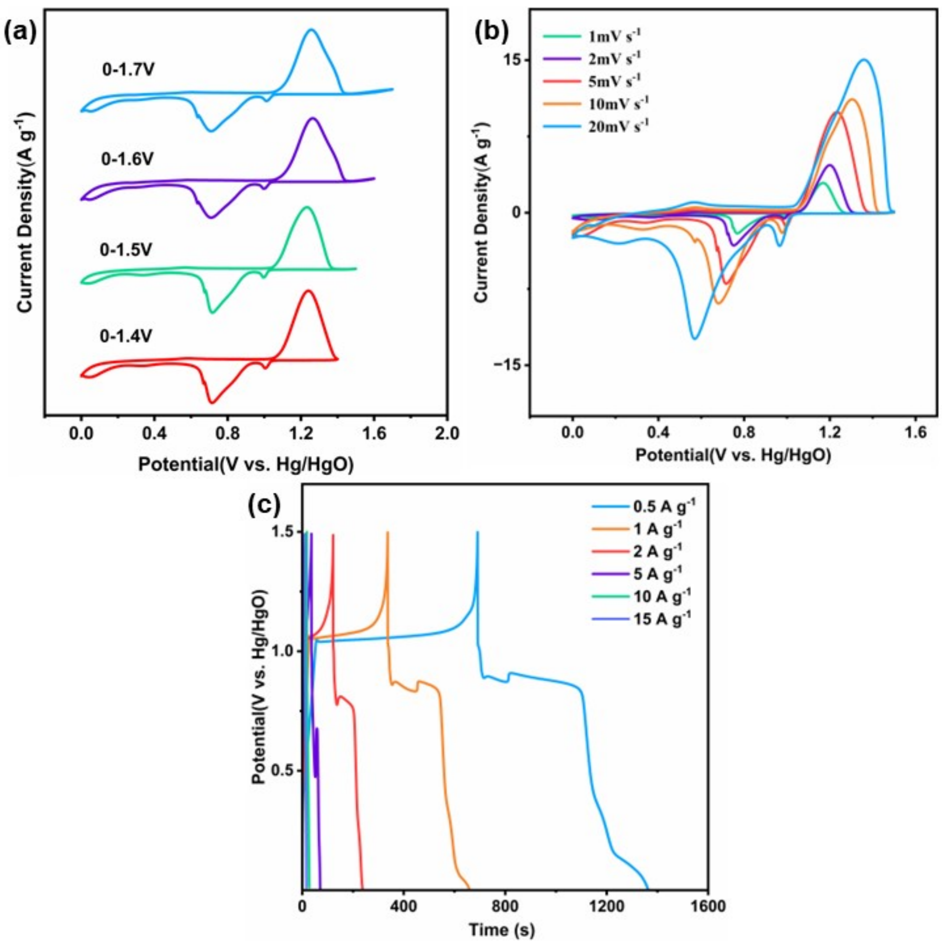

Figure S19. (a) CV curves (5 mV s^{-1}) at various potential windows, (b) CV plots at 1–

20 mV s^{-1}, and (c) GCD curves at 0.5–15 A g^{-1} of the designed NHF–0.03//Bi_2O_3 device.

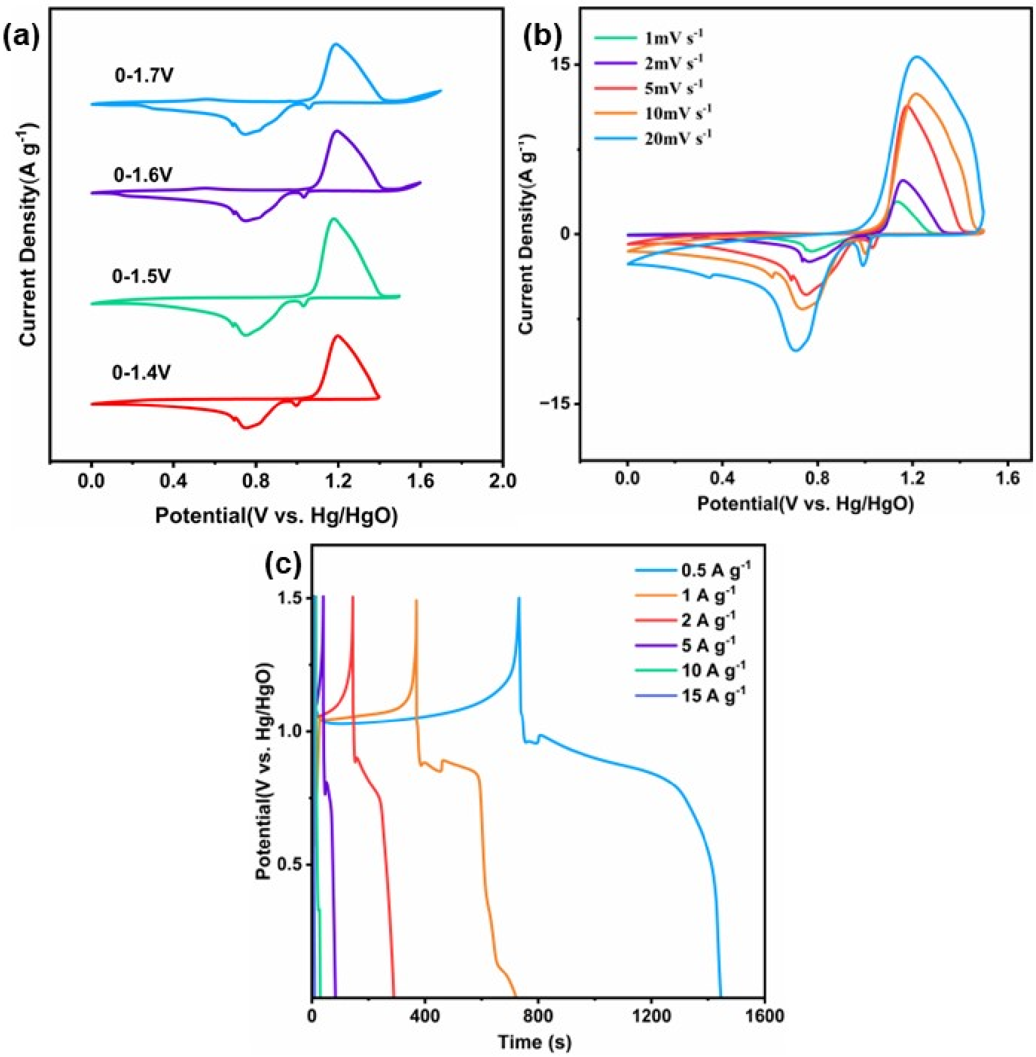

Figure S20. (a) CV curves (5 mV s^{-1}) at various potential windows, (b) CV plots at 1–20 mV s^{-1}, and (c) GCD curves at 0.5–15 A g^{-1} of the designed NHF–0.03// Bi_2O_3 device. (Nickel foam is used as current collector).

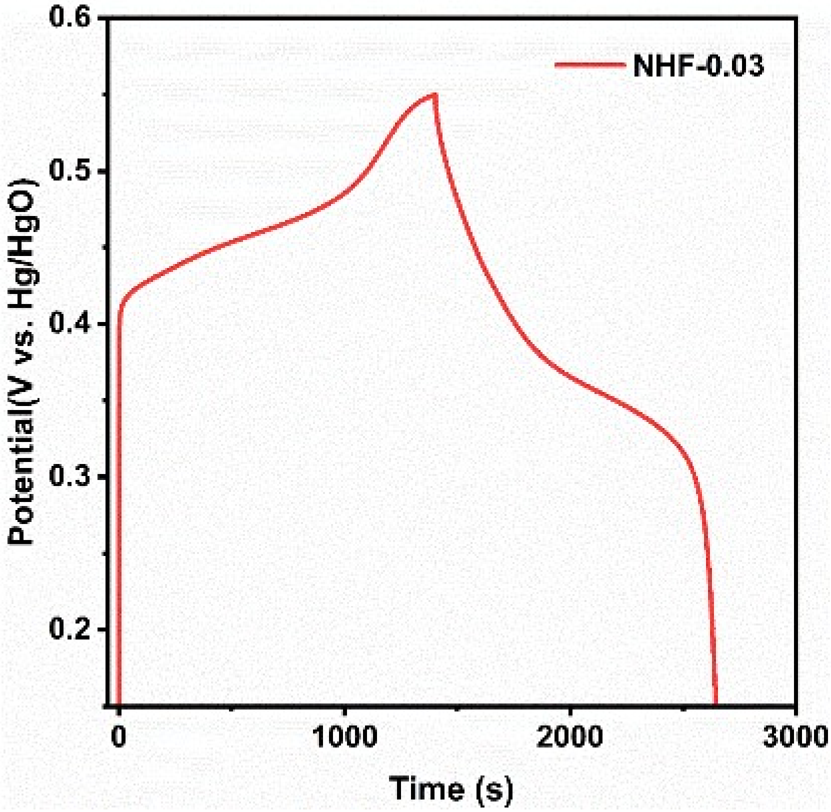

Figure S21. GCD curves spectra at 1A g^{-1} of NHF–0.03 on Ni foam.

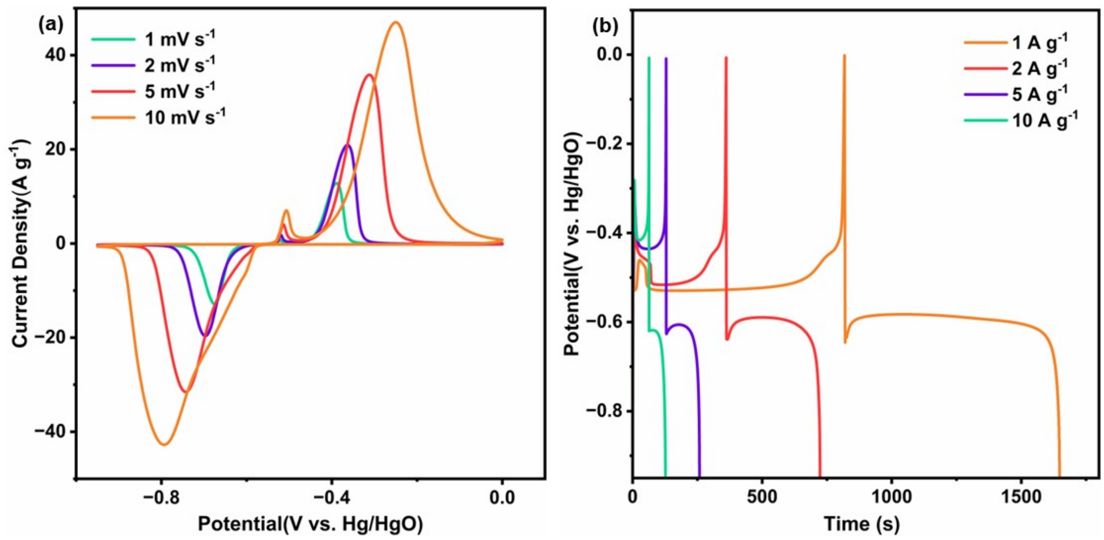

Figure S22. (a) CV plots at 1-10 mV s^{-1} and (b) GCD curves at 1-10 A g^{-1} of Bi_2O_3 on Ni foam.

Table S1. Fe/Ni atomic ratios of NHF-x samples by ICP-OES.

Sample x value	0.01	0.03	0.05
Fe/Ni (Raw material ratio)	0.01	0.03	0.05
Fe/Ni (by ICP-OES)	0.0091	0.0180	0.232

Table S2. Fe^{2+}/ Fe^{3+} and Ni^{2+}/ Ni^{3+} ratio of NHF-x (x=0,0.01,0.03,0.05).

	NHF	NHF–0.01	NHF–0.03	NHF–0.05
Ni^{2+}/ Ni^{3+}	1.212	1.611	1.739	1.749
Fe^{2+}/ Fe^{3+}		1.035	0.991	0.952

Table S3. Charge and discharge time of NHF-0.03 of different numbers of CV cycles.

Cycle numbers / **time**	20	40	60	80
Charge time(s)	1158	874	756	642
Discharge time(s)	673	636	668	633

Table S4. EIS impedance spectrum fitting data for prepared electrodes.

Electrode	Rs(Ω)	Rct(Ω)	Zw($\Omega\ S^{-1/2}$)
NHF	0.98	3.31	0.31
NHF-0.01	1.07	2.22	0.27
NHF-0.03	1.12	1.35	0.25
NHF-0.05	1.10	1.91	0.35

Table S5. F atomic ratios of NHF and NHF–0.03 before and after long-term cycling.

At%（F）	NHF	NHF–0.03
Before cycle	32	33.4
After cycle	1.4	4.3

Table S6. NHF–0.03//AC energy density at different power densities.

	750 W kg^{-1}	1500 W kg^{-1}	3000W kg^{-1}	7500 W kg^{-1}	15000 W kg^{-1}	22500 W kg^{-1}
	55.5 Wh kg^{-1}	48.6 Wh kg^{-1}	44.9 Wh kg^{-1}	41 Wh kg^{-1}	33.6 Wh kg^{-1}	25 Wh kg^{-1}

Table S7. Comparison of energy density and power density of NHF–0.03 //AC ASC with other supercapacitors.

Supercapacitor	**Energy density**	**Power density**	**Ref.**
Co-CH@Mn-Ni$(OH)_2$/ CC//AC	45.8 Wh kg^{-1}	800.0 W kg^{-1}	8
	25.6 Wh kg^{-1}	12800.0 W kg^{-1}	
Co_3O_4@Ni$(OH)_2$//AC	40 Wh kg^{-1}	346.9 W kg^{-1}	9
	14.4 Wh kg^{-1}	3455 W kg^{-1}	
$Co_{0.5}Ni_{0.5}WO_4$//AC	42.2 Wh kg^{-1}	1047.7 W kg^{-1}	10
	23.7 Wh kg^{-1}	9371.4 W kg^{-1}	
rP@rGO//Ni_2P	41.66 Wh kg^{-1}	1200 W kg^{-1}	11
	15.55 Wh kg^{-1}	8000 W kg^{-1}	
$Co_{0.1}Ni_{0.9}P$/CNF/ CC//AC/CC	32.2 Wh kg^{-1}	3500 W kg^{-1}	12
	27 Wh kg^{-1}	14000 W kg^{-1}	
MnO_2@Co-Ni LDH//AC	40.9 Wh kg^{-1}	400 W kg^{-1}	13
	21.3 Wh kg^{-1}	4800 W kg^{-1}	
NHF–0.03//AC	55.5 Wh kg^{-1}	750 W kg^{-1}	This Work
	25 Wh kg^{-1}	22500 W kg^{-1}	

Table S8. NHF–0.03//Bi_2O_3 energy density at different power densities.

	750 W kg^{-1}	1500 W kg^{-1}	3000W kg^{-1}	7500 W kg^{-1}	15000 W kg^{-1}	22500 W kg^{-1}
	102.3 Wh kg^{-1}	101.1 Wh kg^{-1}	72.8 Wh kg^{-1}	54.2 Wh kg^{-1}	31.3 Wh kg^{-1}	25.0 Wh kg^{-1}

Table S9. NHF–0.03//Bi_2O_3 energy density at different power densities.(Nickel foam is used as current collector).

	750 W kg^{-1}	1500 W kg^{-1}	3000W kg^{-1}	7500 W kg^{-1}	15000 W kg^{-1}	22500 W kg^{-1}
	112.6 Wh kg^{-1}	110.0 Wh kg^{-1}	89.0 Wh kg^{-1}	66.6 Wh kg^{-1}	47.7 Wh kg^{-1}	28.1Wh kg^{-1}

References

1. S.-K. Geng, Y. Zheng, S.-Q. Li, H. Su, X. Zhao, J. Hu, H.-B. Shu, M. Jaroniec, P. Chen, Q.-H. Liu and S.-Z. Qiao, Nickel ferrocyanide as a high-performance urea oxidation electrocatalyst, *Nature Energy*, 2021, **6**, 904-912.
2. J. Huang, Y. Li, Y. Zhang, G. Rao, C. Wu, Y. Hu, X. Wang, R. Lu, Y. Li and J. Xiong, Identification of Key Reversible Intermediates in Self-Reconstructed Nickel-Based Hybrid Electrocatalysts for Oxygen Evolution, *Angewandte Chemie International Edition*, 2019, **58**, 17458-17464.
3. W. Lai, L. Ge, H. Li, Y. Deng, B. Xu, B. Ouyang and E. Kan, In situ Raman spectroscopic study towards the growth and excellent HER catalysis of Ni/Ni(OH)2 heterostructure, *International Journal of Hydrogen Energy*, 2021, **46**, 26861-26872.
4. S. Li, Y. Zhang, N. Liu, C. Yu, S.-J. Lee, S. Zhou, R. Fu, J. Yang, W. Guo, H. Huang, J.-S. Lee, C. Wang, T. R. Kim, D. Nordlund, P. Pianetta, X. Du, J. Zhao, Y. Liu and J. Qiu, Operando Revealing Dynamic Reconstruction of NiCo Carbonate Hydroxide for High-Rate Energy Storage, *Joule*, 2020, **4**, 673-687.

5. P. Tang, P. Gao, X. Cui, Z. Chen, Q. Fu, Z. Wang, Y. Mo, H. Liu, C. Xu, J. Liu, J. Yan and S. Passerini, Covalency Competition Induced Active Octahedral Sites in Spinel Cobaltites for Enhanced Pseudocapacitive Charge Storage, *Advanced Energy Materials*, 2022, **12**, 2102053.
6. P. Gao, P. Tang, Y. Mo, P. Xiao, W. Zhou, S. Chen, H. Dong, Z. Li, C. Xu and J. Liu, Covalency competition induced selective bond breakage and surface reconstruction in manganese cobaltite towards enhanced electrochemical charge storage, *Green Energy & Environment*, 2024, **9**, 909-918.
7. P. Tang, W. Tan, G. Deng, Y. Zhang, S. Xu, Q. Wang, G. Li, J. Zhu, Q. Dou and X. Yan, Understanding Pseudocapacitance Mechanisms by Synchrotron X-ray Analytical Techniques, *ENERGY & ENVIRONMENTAL MATERIALS*, 2023, **6**, e12619.
8. G. Wang, Y. Ding, Z. Xu, G. Wang, Z. Li and Z. Yan, Co_3O_4@Mn-$Ni(OH)_2$ core–shell heterostructure for hybrid supercapacitor electrode with high utilization, *Chemical Engineering Journal*, 2023, **469**, 143984.
9. X. Bai, Q. Liu, J. Liu, H. Zhang, Z. Li, X. Jing, P. Liu, J. Wang and R. Li, Hierarchical Co_3O_4@$Ni(OH)_2$ core-shell nanosheet arrays for isolated all-solid state supercapacitor electrodes with superior electrochemical performance, *Chemical Engineering Journal*, 2017, **315**, 35-45.
10. B. Huang, H. Wang, S. Liang, H. Qin, Y. Li, Z. Luo, C. Zhao, L. Xie and L. Chen, Two-dimensional porous cobalt–nickel tungstate thin sheets for high performance supercapattery, *Energy Storage Materials*, 2020, **32**, 105-114.
11. N. Parveen, M. Hilal and J. I. Han, Newly Design Porous/Sponge Red Phosphorus@Graphene and Highly Conductive Ni_2P Electrode for Asymmetric Solid State Supercapacitive Device With Excellent Performance, *Nano-Micro Letters*, 2020, **12**, 25.
12. N. Zhang, Y. Li, J. Xu, J. Li, B. Wei, Y. Ding, I. Amorim, R. Thomas, S. M. Thalluri, Y. Liu, G. Yu and L. Liu, High-Performance Flexible Solid-State Asymmetric Supercapacitors Based on Bimetallic Transition Metal Phosphide Nanocrystals, *ACS Nano*, 2019, **13**, 10612-10621.
13. H. Luo, B. Wang, T. Liu, F. Jin, R. Liu, C. Xu, C. Wang, K. Ji, Y. Zhou, D. Wang and S. Dou, Hierarchical design of hollow Co-Ni LDH nanocages strung by MnO_2 nanowire with enhanced pseudocapacitive properties, *Energy Storage Materials*, 2019, **19**, 370-378.